

Algorithm to estimate the Hurst exponent of high-dimensional fractals

Anna Carbone

*Physics Department, Politecnico di Torino,
Corso Duca degli Abruzzi 24,
I-10129 Torino, Italy*

(Dated: February 9, 2022)

Abstract

We propose an algorithm to estimate the Hurst exponent of high-dimensional fractals, based on a generalized high-dimensional variance around a moving average low-pass filter. As working examples, we consider rough surfaces generated by the Random Midpoint Displacement and by the Cholesky-Levinson Factorization algorithms. The surrogate surfaces have Hurst exponents ranging from 0.1 to 0.9 with step 0.1, and different sizes. The computational efficiency and the accuracy of the algorithm are also discussed.

PACS numbers: 05.10.-a, 05.40.-a, 05.45.Df, 68.35.Ct

I. INTRODUCTION

The scaling properties of random curves and surfaces can be quantified in terms of the Hurst exponent H , a parameter defined in the framework of the fractional Brownian walks introduced in [1]. A fractional Brownian function $f(\mathbf{r}) : \mathbb{R}^d \rightarrow \mathbb{R}$, is characterized by a variance σ_H^2 :

$$\sigma_H^2 = \langle [f(\mathbf{r} + \boldsymbol{\lambda}) - f(\mathbf{r})]^2 \rangle \propto \|\boldsymbol{\lambda}\|^\alpha \quad \text{with} \quad \alpha = 2H, \quad (1)$$

with $\mathbf{r} = (x_1, x_2, \dots, x_d)$, $\boldsymbol{\lambda} = (\lambda_1, \lambda_2, \dots, \lambda_d)$ and $\|\boldsymbol{\lambda}\| = \sqrt{\lambda_1^2 + \lambda_2^2 + \dots + \lambda_d^2}$; a power spectrum S_H :

$$S_H \propto \|\boldsymbol{\omega}\|^{-\beta} \quad \text{with} \quad \beta = d + 2H, \quad (2)$$

with $\boldsymbol{\omega} = (\omega_1, \omega_2, \dots, \omega_d)$ the angular frequency, $\|\boldsymbol{\omega}\| = \sqrt{\omega_1^2 + \omega_2^2 + \dots + \omega_d^2}$; a number of objects N_H of characteristic size ϵ needed to cover the fractal:

$$N_H \propto \epsilon^{-D} \quad \text{with} \quad D = d + 1 - H, \quad (3)$$

D being the fractal dimension of $f(\mathbf{r})$. The Hurst exponent ranges from 0 to 1, taking the values $H = 0.5$, $H > 0.5$ and $H < 0.5$ respectively for uncorrelated, correlated and anticorrelated Brownian functions.

The application of fractal concepts, through the estimate of H , has been proven useful in a variety of fields. For example in $d = 1$, heartbeat intervals of healthy and sick hearts are discriminated on the basis of the value of H [2, 3]; the stage of financial market development is related to the correlation degree of return and volatility series [4]; coding and non coding regions of genomic sequences have different correlation degrees [5]; climate models are validated by analyzing long-term correlation in atmospheric and oceanographic series [6, 7]. In $d \geq 2$ fractal measures are used to model and quantify stress induced morphological transformation [8]; isotropic and anisotropic fracture surfaces [9, 10, 11, 12, 13]; static friction between materials dominated by hard core interactions [14]; diffusion [15, 16] and transport [17, 18] in porous and composite materials; mass fractal features in wet/dried gels [19] and in physiological organs (e.g. lung) [20]; hydrophobicity of surfaces with hierarchic structure undergoing natural selection mechanism [21] and solubility of nanoparticles [22]; digital elevation models [23] and slope fits of planetary surfaces [24].

A number of fractal quantification methods - based on the Eqs. (1-3) or on variants of these relationships - like Rescaled Range Analysis (R/S), Detrended Fluctuation Analysis (DFA), Detrending Moving Average Analysis (DMA), Spectral Analysis, have been thus proposed to accomplish accurate and fast estimates of H in order to investigate correlations at different scales in $d = 1$. A comparatively small number of methods able to capture spatial correlations-operating in $d \geq 2$ -have been proposed so far [25, 26, 27, 28, 29, 30, 31, 32]. This work is addressed to develop an algorithm to estimate the Hurst exponent of high-dimensional fractals and thus is intended to capture scaling and correlation properties over space. The proposed method is based on a generalized high-dimensional variance of the fractional Brownian function around a moving average. In Section II, we report the relationships holding for fractals with arbitrary dimension. It is argued that the implementation can be carried out in directed or isotropic mode. We show that the Detrending Moving Average (DMA) method [30, 31, 32] is recovered for $d = 1$. In Section III, the feasibility of the technique is proven by implementing the algorithm on rough surfaces - with different size $N_1 \times N_2$ and Hurst exponent H - generated by the Random Midpoint Displacement (RMD) and by the Cholesky-Levinson Factorization (CLF) methods [33, 34]. The generalized variance is estimated over sub-arrays $n_1 \times n_2$ with different size (“scales”) and then averaged over the whole fractal domain $N_1 \times N_2$. This feature reduces the bias effects due to nonstationarity with an overall increase of accuracy - compared to the two-point correlation function, whose average is calculated over all the fractal. Furthermore - compared to the two-point correlation function, whose implementation is carried out along 1-dimensional lines (e.g. for the fracture problem, the two-point correlation functions are measured along the crack propagation direction and the perpendicular one), the present technique is carried out over d -dimensional structures (e.g. squares in $d = 2$). In Section IV, we discuss accuracy and range of applicability of the method.

II. METHOD

In order to implement the algorithm, the generalized variance σ_{DMA}^2 is introduced:

$$\sigma_{DMA}^2 = \frac{1}{\mathcal{N}} \sum_{i_1=n_1-m_1}^{N_1-m_1} \sum_{i_2=n_2-m_2}^{N_2-m_2} \dots \sum_{i_d=n_d-m_d}^{N_d-m_d} \left[f(i_1, i_2, \dots, i_d) - \tilde{f}_{n_1, n_2, \dots, n_d}(i_1, i_2, \dots, i_d) \right]^2, \quad (4)$$

where $f(i_1, i_2, \dots, i_d) = f(\mathbf{i})$ is a fractional Brownian function defined over a discrete d -dimensional domain, with maximum sizes N_1, N_2, \dots, N_d . It is $i_1 = 1, 2, \dots, N_1$, $i_2 = 1, 2, \dots, N_2$, ..., $i_d = 1, 2, \dots, N_d$. $\mathbf{n} = (n_1, n_2, \dots, n_d)$ defines the sub-arrays ν_d of the fractal domain with maximum values $n_{1max} = \max\{n_1\}$, $n_{2max} = \max\{n_2\}$, ..., $n_{dmax} = \max\{n_d\}$; $m_1 = \text{int}(n_1\theta_1), m_2 = \text{int}(n_2\theta_2), \dots, m_d = \text{int}(n_d\theta_d)$ and $\theta_1, \theta_2, \dots, \theta_d$ are parameters ranging from 0 to 1; $\mathcal{N} = (N_1 - n_{1max}) \cdot (N_2 - n_{2max}) \cdot \dots \cdot (N_d - n_{dmax})$. The function $\tilde{f}_{n_1, n_2, \dots, n_d}(i_1, i_2, \dots, i_d) = \tilde{f}$ is given by:

$$\begin{aligned} \tilde{f}_{n_1, n_2, \dots, n_d}(i_1, i_2, \dots, i_d) &= \frac{1}{n_1 n_2 \dots n_d} \sum_{k_1=-m_1}^{n_1-1-m_1} \sum_{k_2=-m_2}^{n_2-1-m_2} \dots \\ &\dots \sum_{k_d=-m_d}^{n_d-1-m_d} f(i_1 - k_1, i_2 - k_2, \dots, i_d - k_d), \end{aligned} \quad (5)$$

that is an average of f calculated over the sub-arrays ν_d . The Eqs. (4) and (5) are defined for any value of n_1, n_2, \dots, n_d and for any shape of the sub-arrays, however, it is preferable to choose sub-arrays with $n_1 = n_2 = \dots = n_d$ to avoid spurious directionality in the results. The generalized variance σ_{DMA}^2 varies as $(\sqrt{n_1^2 + n_2^2 + \dots + n_d^2})^{2H}$ as a consequence of the property (1) of the fractional Brownian functions.

Upon variation of the parameters $\theta_1, \theta_2, \dots, \theta_d$ in the range $[0, 1]$, the indexes i_1, i_2, \dots, i_d and k_1, k_2, \dots, k_d of the sums in the Eqs. (4) and (5) are accordingly set within ν_d . In particular, (i_1, i_2, \dots, i_d) coincides respectively with: (a) one of the vertices of ν_d for $\theta_1 = \theta_2 = \dots = \theta_d = 0$ and $\theta_1 = \theta_2 = \dots = \theta_d = 1$ or (b) the center of ν_d for $\theta_1 = \theta_2 = \dots = \theta_d = 1/2$. It is worthy of note that the choice $\theta_1 = \theta_2 = \dots = \theta_d = 1/2$ corresponds to the *isotropic* implementation of the algorithm, while $\theta_1 = \theta_2 = \dots = \theta_d = 0$ and $\theta_1 = \theta_2 = \dots = \theta_d = 1$ correspond to the *directed* implementation. For example in $d = 2$, the *isotropic* implementation implies that the variance defined by the Eq. (4) is referred to a moving average \tilde{f} calculated over squares $n_1 \times n_2$ whose center is (i_1, i_2) . Conversely, the *directed* implementation implies that the function \tilde{f} is calculated over squares $n_1 \times n_2$ with one of the vertices in (i_1, i_2) . The *directed* mode is of interest to estimate H in fractals with preferential growth direction, e.g. biological tissues (lung), epitaxial layers, crack propagation in fracture (*anisotropic fractals*). If the fractal is *isotropic* and the accuracy is a priority, the parameters $\theta_1, \theta_2, \dots, \theta_d$ should be preferably taken equal to $1/2$ to achieve the most precise estimate of H . The dependence of the algorithm on θ for $d = 1$ has been discussed in [32].

In order to calculate the Hurst exponent, the algorithm is implemented through the following steps. The moving average \tilde{f} is calculated for different sub-arrays ν_d , by varying n_1, n_2, \dots, n_d from 2 to the maximum values $n_{1max}, n_{2max}, \dots, n_{dmax}$. The values $n_{1max}, n_{2max}, \dots, n_{dmax}$ depend on the maximum size of the fractal domain. In order to minimize the saturation effects due to finite-size, it should be: $n_{1max} \ll N_1$; $n_{2max} \ll N_2$; ...; $n_{dmax} \ll N_d$. These constraints will be further clarified in Section III, where the algorithm is implemented over fractal surfaces with different sizes. For each sub-array ν_d , the corresponding value of σ_{DMA}^2 is calculated and finally plotted on log-log axes.

To elucidate the way the algorithm works, in the following we consider its implementation for $d = 1$ and $d = 2$. The case $d = 1$ reduces to the Detrending Moving Average (DMA) method already used for long-range correlated time series [30, 31, 32].

1-dimensional case:

By posing $d = 1$ in the Eq. (4), one obtains:

$$\sigma_{DMA}^2 = \frac{1}{N_1 - n_{1max}} \sum_{i_1=n_1-m_1}^{N_1-m_1} \left[f(i_1) - \tilde{f}_{n_1}(i_1) \right]^2, \quad (6)$$

where N_1 is the length of the sequence, n_1 is the sliding window and $n_{1max} = \max\{n_1\} \ll N_1$. The quantity $m_1 = \text{int}(n_1\theta_1)$ is the integer part of $n_1\theta_1$ and θ_1 is a parameter ranging from 0 to 1. The relationship (6) defines a generalized variance of the sequence $f(i_1)$ with respect to the function $\tilde{f}_{n_1}(i_1)$:

$$\tilde{f}_{n_1}(i_1) = \frac{1}{n_1} \sum_{k_1=-m_1}^{n_1-1-m_1} f(i_1 - k_1), \quad (7)$$

which is the moving average of $f(i_1)$ over each sliding window of length n_1 . The moving average $\tilde{f}_{n_1}(i_1)$ is calculated for different values of the window n_1 , ranging from 2 to the maximum value n_{1max} . The variance σ_{DMA}^2 is then calculated according to the Eq. (6) and plotted as a function of n_1 on log-log axes. The plot is a straight line, as expected for a power-law dependence of σ_{DMA}^2 on n_1 :

$$\sigma_{DMA}^2 \sim n_1^{2H}. \quad (8)$$

The Eq. (8) allows one to estimate the scaling exponent H of the series $f(i_1)$. Upon variation

of the parameter θ_1 in the range $[0, 1]$, the index k_1 in $\tilde{f}_{n_1}(i_1)$ is accordingly set within the window n_1 . In particular, $\theta_1 = 0$ corresponds to average $f_{n_1}(i_1)$ over all the points to the left of i_1 within the window n_1 ; $\theta_1 = 1$ corresponds to average $f_{n_1}(i_1)$ over all the points to the right of i_1 within the window n_1 ; $\theta_1 = \frac{1}{2}$ corresponds to average $f_{n_1}(i_1)$ with the reference point in the center of the window n_1 .

2-dimensional case

For $d = 2$, the generalized variance defined by the Eq.(4) writes:

$$\sigma_{DMA}^2 = \frac{1}{(N_1 - n_{1max})(N_2 - n_{2max})} \sum_{i_1=n_1-m_1}^{N_1-m_1} \sum_{i_2=n_2-m_2}^{N_2-m_2} \left[f(i_1, i_2) - \tilde{f}_{n_1, n_2}(i_1, i_2) \right]^2, \quad (9)$$

with $\tilde{f}_{n_1, n_2}(i_1, i_2)$ given by:

$$\tilde{f}_{n_1, n_2}(i_1, i_2) = \frac{1}{n_1 n_2} \sum_{k_1=-m_1}^{n_1-1-m_1} \sum_{k_2=-m_2}^{n_2-1-m_2} f(i_1 - k_1, i_2 - k_2). \quad (10)$$

The average \tilde{f} is calculated over sub-arrays with different size $n_1 \times n_2$. The next step is the calculation of the difference $f(i_1, i_2) - \tilde{f}_{n_1, n_2}(i_1, i_2)$ for each sub-array $n_1 \times n_2$. A log-log plot of σ_{DMA}^2 :

$$\sigma_{DMA}^2 \sim \left[\sqrt{n_1^2 + n_2^2} \right]^{2H} \sim s^H. \quad (11)$$

as a function of $s = n_1^2 + n_2^2$, yields a straight line with slope H .

Depending upon the values of the parameters θ_1 and θ_2 , entering the quantities $m_1 = \text{int}(n_1\theta_1)$ and $m_2 = \text{int}(n_2\theta_2)$ in the Eqs. (9,10), the position of (k_1, k_2) and (i_1, i_2) can be varied within each sub-array. (i_1, i_2) coincides with a vertex of the sub-array if: (i) $\theta_1 = 0, \theta_2 = 0$; (ii) $\theta_1 = 0, \theta_2 = 1$; (iii) $\theta_1 = 1, \theta_2 = 0$; (iv) $\theta_1 = 1, \theta_2 = 1$ (*directed implementation*). The choice $\theta_1 = \theta_2 = 1/2$ corresponds to take the point (i_1, i_2) coinciding with the center of each sub-array $n_1 \times n_2$ (*isotropic implementation*) [41].

III. RESULTS

In order to test feasibility and robustness of the proposed method, synthetic rough surfaces with assigned Hurst exponents have been generated by the Random Midpoint Displacement

(RMD) algorithm and by the Cholesky-Levinson Factorization (CLF) method [33, 34]. The widespread use of the RMD algorithm is based on the trade-off of its fast, simple and efficient implementation to its limited accuracy especially for $H \ll 0.5$ and $H \gg 0.5$. Conversely, the Cholesky-Levinson Factorization method is one of the most accurate techniques to generate $1d$ and $2d$ fractional Brownian functions, at the expenses of a more complex implementation structure [42].

In Fig. 1, the log-log plots of σ_{DMA}^2 as a function of s are shown for the synthetic fractal surfaces generated by the RMD (circles) and by the CLF method (squares). The surfaces have Hurst exponents H_{in} ranging from 0.1 to 0.9 with step 0.1. The domain sizes are respectively $N_1 \times N_2 = 256 \times 256$ (a), $N_1 \times N_2 = 1024 \times 1024$ (b) and $N_1 \times N_2 = 4096 \times 4096$ (c). The dashed lines show the behavior that should be exhibited by variances varying exactly as $s^{H_{in}}$ over the entire range of scales. The plots of σ_{DMA}^2 as a function s are in good agreement with the behavior expected on the basis of the Eq. (11). The quality of the fits is higher for the surfaces generated by the CLF method, confirming that the RMD algorithm synthesizes less accurate fractals. By comparing the results of the simulation (symbols) to the straight lines corresponding to full linearity over the whole range (dashed), deviations from the full linearity can be observed especially for the small surfaces at the extremes of the scale. A plot of the slopes for the fractal surfaces generated by the CLF algorithm is shown in Fig. 2 for different sizes of the fractal domain. A detailed discussion of the origin of the deviations at low and large scales is reported in the Section IV.

Finally, we also show three examples of digital images currently mapped to fractal surfaces with reference to the color intensity i.e. to the levels of Red, Green and Blue (RGB). The Hurst exponents estimated by the proposed method are respectively $H = 0.1$ (a), $H = 0.5$ (b) and $H = 0.9$ (c) for the images in Fig. 3.

IV. DISCUSSION

The proposed algorithm is characterized by short execution time and ease of implementation. By considering the case $d = 2$, the function $\tilde{f}_{n_1, n_2}(i_1, i_2)$ is indeed simply obtained by summing the values of $f(i_1, i_2)$ over each sub-array $n_1 \times n_2$. Then the sum is updated at each step by adding the last and discarding the first row (column) of each sliding array $n_1 \times n_2$. For higher dimensions, the sum is updated at each step by adding and discarding a

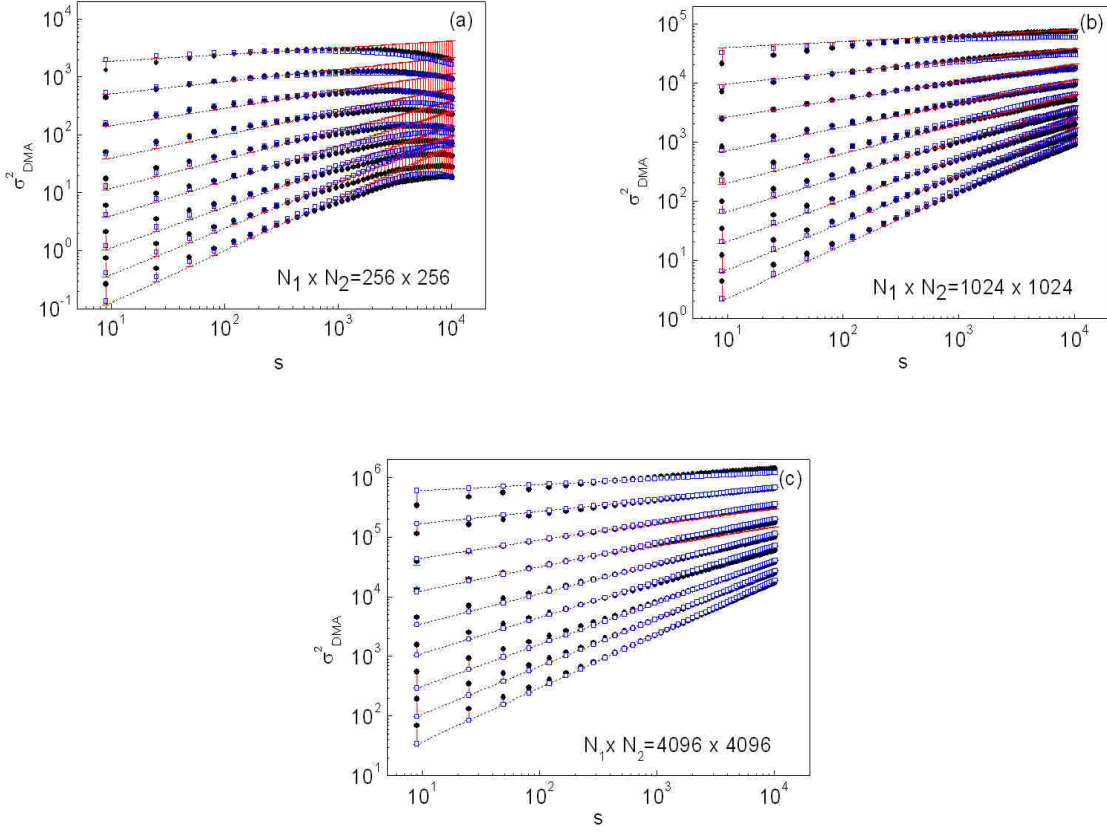


FIG. 1: (Color online) Log-log plot of σ_{DMA}^2 for fractal surfaces respectively with size $N_1 \times N_2 = 256 \times 256$ (a), $N_1 \times N_2 = 1024 \times 1024$ (b) and $N_1 \times N_2 = 4096 \times 4096$ (c). The data refer to fractal surfaces generated by the RMD (circles) and by the CLF (squares) methods. The Hurst exponent H_{in} - input of the RMD and the CLF algorithm - varies from 0.1 to 0.9 with step 0.1. The results correspond to the isotropic implementation, i.e. with the parameters $\theta_1 = \theta_2 = 1/2$ in the Eq.(9). The dashed lines represent the behavior expected for full linearity, i.e. the log-log plot of curves varying as $s^{H_{in}}$. It is worthy of note that the CLF data are closer to the full-linearity compared to the RMD ones.

$d - 1$ dimensional set of each array $n_1 \times n_2 \times \dots \times n_d$. The algorithm does not use arbitrary parameters, the computation simply relying on averages of f . We will now argue on the origin of the deviations at small and at large scales.

Deviations at large scales. The deviations from the linearity at large scales, leading to the saturation of the σ_{DMA}^2 , are due to finite size effects. The small surfaces do not contain enough data to make the evaluation of the scaling law over the sub-arrays statistically

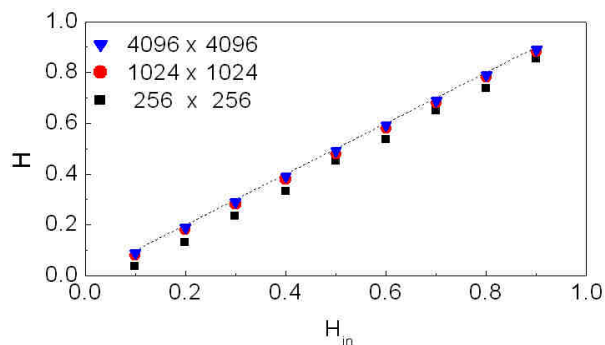


FIG. 2: (Color online) Plot of the values of H obtained by linear fit of the curves shown in Fig. 1 (a), (b), (c). The data refer to the fractal surfaces generated by the Cholesky-Levinson Factorization method (squares). The dashed lines represent the ideal behavior: $H = H_{in}$.

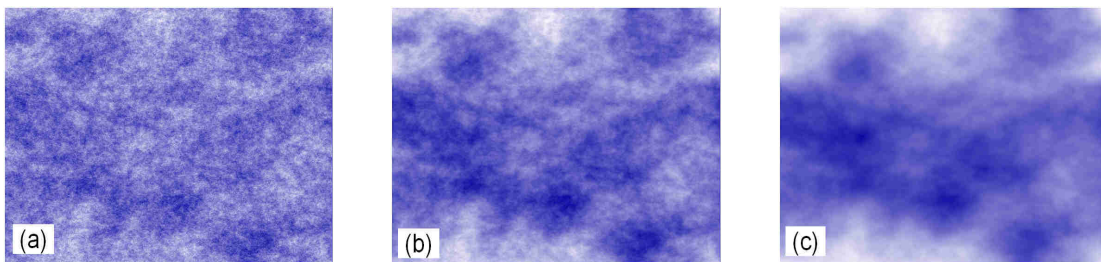


FIG. 3: (Color online). Cloudy sky images respectively with Hurst exponent $H = 0.1$ (a), $H = 0.5$ (b) and $H = 0.9$ (c). Such heterogeneous images are represented as fractal surfaces by mapping the color intensity (RGB content).

meaningful. By comparing the data in Figs. 1 (a), (b), (c), one can note that the saturation effect decreases upon increasing the size $N_1 \times N_2$ of the fractal surface. The finite size effects become negligible when the conditions $n_{1max} \ll N_1$; $n_{2max} \ll N_2$; ...; $n_{dmax} \ll N_d$ are fulfilled.

Deviations occurring at small scales. The deviations occurring at low scales are related to the departure of the low-pass filter from the ideality. This problem also occurs with one-dimensional fractals (time series) resulting in the quite generally reported overestimation of H in anticorrelated signals and underestimation of H in correlated signals [35, 36, 37, 38, 39]. We will discuss the origin of these deviations by means of the filter transfer function $\mathcal{H}_{\mathcal{T}}(\omega)$

[40]. The algorithm is based on a generalized variance of the function f with respect to \tilde{f} . The function \tilde{f} is the output of a *low-pass filter* driven by f , with impulse response a box-car function. In the Appendix, the transfer function $\mathcal{H}_{\mathcal{T}}(\omega)$ of \tilde{f} is explicitly calculated and shown in Fig.(4) for $d = 2$. For an *ideal* low-pass filter, the transfer function should be one or zero respectively at frequencies lower or higher than the cut-off frequency. However, in real low-pass filters, at frequencies lower than the cut-off frequency, all the components of the signal suffer some attenuation but $\omega = 0$. The cut-off frequencies of $\mathcal{H}_{\mathcal{T}}(\omega)$ are $\omega_i = \pi/\tau_i$, i.e. the first zeroes of the functions $\sin \omega_i \tau_i / \omega_i \tau_i$ in the Eq. (A.4). Moreover, in real filters, at frequencies higher than π/τ_i , due to the presence of the sidelobes, components of the signals lying in the bands $(\pi/\tau_i, 2\pi/\tau_i)$; $(2\pi/\tau_i, 3\pi/\tau_i)$; ..., are not fully filtered out. As a result, the function \tilde{f} contains: (a) less components with frequency lower than $\omega_i = \pi/\tau_i$ and (b) more components with frequency higher than $\omega_i = \pi/\tau_i$ compared to what it would be expected with an ideal low-pass filter. The lack of low-frequency components depends on the central lobe, while the excess of high-frequency components depends on the side lobes. The excess of high-frequency components results in a smaller value of the difference $f - \tilde{f}$, i.e. in a decrease of σ_{DMA}^2 and, thus, in an increase of the slope of the log-log plot. Conversely, the lack of low-frequency components results in a larger value of the difference $f - \tilde{f}$, i.e. in an increase of σ_{DMA}^2 and, thus, in a decrease of the slope of the log-log plot. The two effects are more relevant with smaller values of the scales, when the filter nonideality is greater. Moreover, as one can deduce from the Eqs. (2) and (A.6), the effect of the side lobes dominates in high-frequency rich fractals with $H < 0.5$, while the effect of the central lobe is dominant in fractals with $H > 0.5$, rich of low-frequency components.

In order to gain further insight in the above theoretical arguments, we report in Table I the slopes H_I , H_{II} and H_{III} of the curves (squares) plotted in Fig. 1 (b)) over different ranges. The slopes have been calculated by linear fit respectively over the ranges $10 \leq s \leq 100$ (H_I), $10 \leq s \leq 1000$ (H_{II}) and $10 \leq s \leq 10000$ (H_{III}). The relative errors $\Delta H = (H - H_{in})/H_{in}$ are given respectively in the 3rd, 5th and 7th columns. The slope H_I is greater than the expected value H_{in} . The slope H_{II} is overestimated for $H = 0.1$ and $H = 0.2$ and underestimated for $H > 0.2$. The slope H_{III} is underestimated since the effects of the finite-size of the fractal domain play a dominant role.

We address the question if the artifacts due to the filter nonideality described above might be corrected somehow. In the remaining of this section, we will thus consider the use

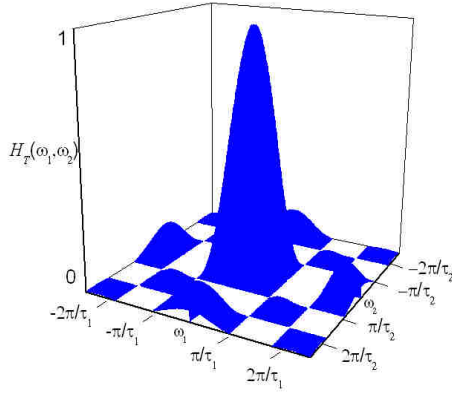


FIG. 4: (Color online) Plot of the transfer function $\mathcal{H}_{\mathcal{T}}(\omega_1, \omega_2)$.

TABLE I: Slopes H_I , H_{II} , H_{III} and relative errors ΔH_I , ΔH_{II} , ΔH_{III} of the curves plotted in Fig. 1(b) (squares). The slopes have been calculated by linear fit respectively over the ranges: $10 \leq s \leq 100$ (H_I), $10 \leq s \leq 1000$ (H_{II}) and $10 \leq s \leq 10000$ (H_{III}). The errors ΔH_I , ΔH_{II} , ΔH_{III} are calculated as $\Delta H = (H - H_{in})/H_{in}$.

H_{in}	H_I	ΔH_I	H_{II}	ΔH_{II}	H_{III}	ΔH_{III}
0.1	0.1346	$+3.46 \cdot 10^{-1}$	0.1073	$+7.30 \cdot 10^{-2}$	0.0718	$-2.822 \cdot 10^{-1}$
0.2	0.2272	$+1.36 \cdot 10^{-1}$	0.2050	$+2.50 \cdot 10^{-2}$	0.1700	$-1.500 \cdot 10^{-1}$
0.3	0.3233	$+7.77 \cdot 10^{-2}$	0.2995	$-1.67 \cdot 10^{-3}$	0.2716	$-9.467 \cdot 10^{-2}$
0.4	0.4205	$+5.12 \cdot 10^{-2}$	0.3970	$-7.50 \cdot 10^{-3}$	0.3691	$-7.725 \cdot 10^{-2}$
0.5	0.5178	$+3.56 \cdot 10^{-2}$	0.4973	$-5.40 \cdot 10^{-3}$	0.4752	$-4.960 \cdot 10^{-2}$
0.6	0.6171	$+2.85 \cdot 10^{-2}$	0.5973	$-4.50 \cdot 10^{-3}$	0.5617	$-6.383 \cdot 10^{-2}$
0.7	0.7185	$+2.64 \cdot 10^{-2}$	0.6956	$-6.29 \cdot 10^{-3}$	0.6770	$-3.286 \cdot 10^{-2}$
0.8	0.8207	$+2.58 \cdot 10^{-2}$	0.7999	$-1.25 \cdot 10^{-4}$	0.7659	$-4.263 \cdot 10^{-2}$
0.9	0.9253	$+2.81 \cdot 10^{-2}$	0.8999	$-1.11 \cdot 10^{-4}$	0.8679	$-3.567 \cdot 10^{-2}$

of *windows* whose general effect is to increase the width of the central lobe while reducing those of the sidelobes of the function $\mathcal{H}_{\mathcal{T}}(\omega)$ (a detailed description of these methods can be found in [40]). By restricting our discussion to the present technique, the correction is performed by using the following variant of the relationship (5):

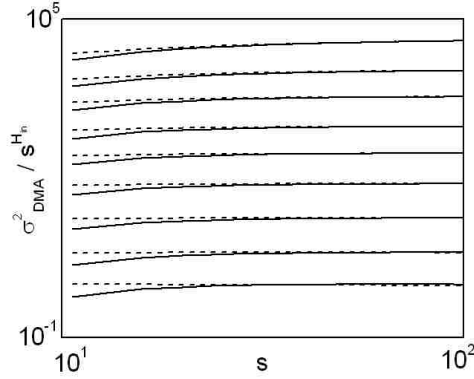


FIG. 5: (Color online) Plot of the function σ_{DMA}^2 with \tilde{f} defined by the Eq. (4) (solid lines) and \tilde{f}^* defined by the Eq. (12) (dashed lines). It can be noted that the deviations of the slope at small scales are reduced by the use of \tilde{f}^* implying a corresponding reduction of the relative error ΔH_I of two orders of magnitude.

$$\begin{aligned} \tilde{f}_{n_1, n_2, \dots, n_d}^*(i_1, i_2, \dots, i_d) = & (1 - \alpha) f_{n_1, n_2, \dots, n_d}(i_1, i_2, \dots, i_d) \\ & + \alpha \tilde{f}_{n_1, n_2, \dots, n_d}(i_1 - 1, i_2 - 1, \dots, i_d - 1), \end{aligned} \quad (12)$$

where $\alpha = n_1 n_2 \dots n_d / [(n_1 + 1)(n_2 + 1) \dots (n_d + 1)]$. The Eq. (12) reduces for $d = 1$ to the exponentially weighted moving average (EWMA). In practice, the difference between the Eq. (5) and the Eq. (12) is that the function \tilde{f}^* places more importance to the data around the point i_1, i_2, \dots, i_d . This is achieved by assigning to the function a weight $(1 - \alpha)$, while all the other values are summed together and weighted by α . In Fig. 5, we show the ratio $\sigma_{DMA}^2 / s^{H_{in}}$ obtained by implementing the algorithm respectively with the function \tilde{f} (solid lines) and \tilde{f}^* (dashed lines) in the range $10 \leq s \leq 100$. The ratio $\sigma_{DMA}^2 / s^{H_{in}}$ is noticeably closer to a constant value when the function \tilde{f} is replaced by \tilde{f}^* , with a corresponding reduction of two orders of magnitude in the relative error ΔH_I .

V. CONCLUSION

We have put forward an algorithm to estimate the Hurst exponent of fractals with arbitrary dimension, based on the high-dimensional generalized variance σ_{DMA}^2 defined by the

Eq. (4).

The methods currently used to estimate the Hurst exponent of high-dimensional fractals are based on: (i) $1-d$ two-point correlation and structure functions operated along different directions, (ii) high- d Fourier and wavelet transforms [9, 10, 11, 12, 13, 29]. The advantage of the methods (i) is the ease of implementation. Their drawback is the limited accuracy due to biases and nonstationarities, being these functions calculated over the entire fractal domain. The methods (ii) are more accurate, however their implementation is complicated especially for data set with limited extension. The generalized variance σ_{DMA}^2 is “scaled”, meaning that it is calculated over sub-arrays of the whole fractal domain by means of the function \tilde{f} . The “scales” are set by the size of the sub-arrays $n_1 \times n_2 \times \dots \times n_d$. Therefore, the proposed method exhibits at the same time: (a) ease of implementation, being based on a variance-like approach and (b) high accuracy, being calculated over scaled sub-arrays rather than on the whole fractal domain.

A further important feature of the proposed algorithm is that it can be implemented “isotropically” or in “directed” mode to accomplish estimates of H in fractals having preferential growth direction e.g. biological tissues, epitaxial layers or in crack propagation in fracture. The *isotropic implementation* is obtained by taking $\theta_1 = \theta_2 = \dots = \theta_d = 1/2$ in the Eq. (4). This choice implies that the reference point (i_1, i_2, \dots, i_d) of the moving average lies in the center of each sub-array $n_1 \times n_2 \times \dots \times n_d$ and thus \tilde{f} is calculated by summing the values of f around (i_1, i_2, \dots, i_d) . Conversely, to implement the algorithm in a preferential direction (*directed implementation*), the reference point must be coincident with one of extremes of the segment n_1 , or with one of the vertices of the square grid $n_1 \times n_2$ or of the d -dimensional array $n_1 \times n_2 \times \dots \times n_d$. The directed implementation can be performed by choosing for example $\theta_1 = \theta_2 = \dots = \theta_d = 0$.

Further generalizations of the proposed method can be envisaged for applications to the analysis of time-dependent spatial correlations in $d \geq 2$.

APPENDIX: TRANSFER FUNCTION OF \tilde{f}

The function \tilde{f} , defined by the Eq. (5), corresponds to the discrete form of the integral:

$$\begin{aligned} \tilde{f}(x_1, x_2, \dots, x_d) &= \frac{1}{\tau_1 \tau_2 \dots \tau_d} \int_{x_1 - \tau_1}^{x_1} dx'_1 \\ &\int_{x_2 - \tau_2}^{x_2} dx'_2 \dots \int_{x_d - \tau_d}^{x_d} dx'_d f(x'_1, x'_2, \dots, x'_d) \end{aligned} \quad (\text{A.1})$$

where for the sake of simplicity we have considered the case $\theta_1 = \theta_2 = \dots = \theta_d = 0$.

The Eq. (A.1) can be rewritten as a convolution integral:

$$\begin{aligned} \tilde{f}(x_1, x_2, \dots, x_d) &= \frac{1}{\tau_1 \tau_2 \dots \tau_d} \int_{-\infty}^{\infty} dx_1^* U\left(\frac{x_1^*}{\tau_1}\right) \int_{-\infty}^{\infty} dx_2^* U\left(\frac{x_2^*}{\tau_2}\right) \dots \\ &\dots \int_{-\infty}^{\infty} dx_d^* U\left(\frac{x_d^*}{\tau_d}\right) f(x_1 - x_1^*, x_2 - x_2^*, \dots, x_d - x_d^*) \end{aligned} \quad (\text{A.2})$$

with the convolution kernels given by the boxcar function:

$$U(x_i^*/\tau_i) = \begin{cases} 1 & \text{for } 0 < x_i^*/\tau_i < 1 \\ 0 & \text{elsewhere .} \end{cases}$$

The transfer function can be calculated as follows:

$$\begin{aligned} \mathcal{H}_{\mathcal{T}}(\omega_1, \omega_2, \dots, \omega_d) &= \frac{1}{\tau_1 \tau_2 \dots \tau_d} \int_0^{\tau_1} dx_1 \int_0^{\tau_2} dx_2 \dots \\ &\int_0^{\tau_d} dx_d \exp[-i2\pi(\omega_1 x_1 + \omega_2 x_2 + \dots + \omega_d x_d)] \end{aligned} \quad (\text{A.3})$$

that can be written as:

$$\mathcal{H}_{\mathcal{T}}(\omega_1, \omega_2, \dots, \omega_d) = \prod_{i=1}^d \frac{\sin \omega_i \tau_i}{\omega_i \tau_i} \quad (\text{A.4})$$

that is thus d -times the function $\sin \omega_i \tau_i / \omega_i \tau_i$.

The Fourier transform $\tilde{\mathcal{F}}$ of the function \tilde{f} can be obtained by means of the following relationship:

$$\tilde{\mathcal{F}}(\omega_1, \omega_2, \dots, \omega_d) = \mathcal{H}_{\mathcal{T}}(\omega_1, \omega_2, \dots, \omega_d) \mathcal{F}(\omega_1, \omega_2, \dots, \omega_d) \quad (\text{A.5})$$

where $\mathcal{F}(\omega_1, \omega_2, \dots, \omega_d)$ is the Fourier transform of the function $f(x_1, x_2, \dots, x_d)$.

The power spectrum \tilde{S} of the function \tilde{f} is given by:

$$\tilde{S}(\omega_1, \omega_2, \dots, \omega_d) = |\mathcal{H}_T(\omega_1, \omega_2, \dots, \omega_d)|^2 S(\omega_1, \omega_2, \dots, \omega_d) \quad (\text{A.6})$$

where $S(\omega_1, \omega_2, \dots, \omega_d)$ is the power spectrum of the function $f(x_1, x_2, \dots, x_d)$.

-
- [1] B. B. Mandelbrot and J. W. Van Ness, *SIAM Rev.* **4**, 422 (1968).
 - [2] S. Thurner, M. C. Feurstein, and M. C. Teich, *Phys. Rev. Lett.* **80**, 1544 (1998).
 - [3] A. L. Goldberger, L. A. N. Amaral, J. M. Hausdorff, P. Ch. Ivanov, C.-K. Peng, and H. E. Stanley, *Proc. Natl. Acad. Sci.* **99**, 2466 (2002).
 - [4] T. Di Matteo, T. Aste, M. M. Dacorogna, *J. Banking & Finance* **29**, 827 (2005).
 - [5] C. K. Peng, S. V. Buldyrev, S. Havlin, M. Simons, H. E. Stanley, and A. L. Goldberger, *Phys. Rev. E* **49**, 1685 (1994).
 - [6] Y. Ashkenazy, D. Baker, H. Gildor, S. Havlin, *Geophys. Res. Lett.* **30**, 2146 (2003).
 - [7] P. Huybers, W. Curry, *Nature* **441**, 7091 (2006).
 - [8] D. L. Blair and A. Kudrolli, *Phys. Rev. Lett.* **94**, 166107 (2005).
 - [9] L. Ponson, D. Bonamy, and E. Bouchaud, *Phys. Rev. Lett.* **96**, 035506 (2006).
 - [10] A. Hansen, G. G. Batrouni, T. Ramstad and J. Schmittbuhl, *Phys. Rev. E* **75**, 030102(R) (2007).
 - [11] E. Bouchbinder, I. Procaccia, S. Santucci, and L. Vionel, *Phys. Rev. Lett.* **96**, 055509 (2006).
 - [12] J. Schmittbuhl, F. Renard, J. P. Gratier, and R. Toussaint, *Phys. Rev. Lett.* **93**, 238501 (2004).
 - [13] S. Santucci, K.J. Maloy, A. Delaplace, et al. , *Phys. Rev. E* **75**, 016104 (2007).
 - [14] J.B. Sokoloff, *Phys. Rev. E* **73**, 016104 (2006).
 - [15] P. Levitz, D. S. Grebenkov, M. Zinsmeister, K. M. Kolwankar and B. Sapoval, *Phys. Rev. Lett.*, **96**, 180601 (2006).
 - [16] K. Malek and M.O. Coppens, *Phys. Rev. Lett.* **87**, 125505 (2001).
 - [17] E. N. Oskoe and M. Sahimi, *Phys. Rev. B* **74**, 045413 (2006).
 - [18] M. Filoche and B. Sapoval, *Phys. Rev. Lett.* **84**, 5776 (2000).
 - [19] D. R. Vollet, D. A. Donati, A. Ibanez Ruiz, and F. R. Gatto, *Phys. Rev. B* **74**, 024208 (2006).

- [20] B. Suki, A.-L. Barabasi, Z. Hantos, F. Petak, and H. E. Stanley, *Nature* **368**, 615 (1994).
- [21] C. Yang, U. Tartaglino and B. N. J. Person, *Phys. Rev. Lett.* **97**, 16103 (2006).
- [22] A. Mihranyan, M. Stromme, *Surf. Sc.* **601**, 315 (2007).
- [23] P. E. Fisher and N. J. Tate, *Prog. in Phys. Geography* **30**, 467 (2006)
- [24] A. K. Sultan-Salem, G. L. Tyler, *J. of Geophys. Res.-Planets* **111**, E06S07 (2006).
- [25] S. Davies and P. Hall, *J. Royal Stat. Soc.* **61**, 147, (1999).
- [26] G. Rangarajan and M. Ding, *Phys. Rev. E* **61**, 004991 (2000).
- [27] J. Alvarez-Ramirez, J. C. Echeverria, I. Cervantes, E. Rodriguez, *Physica A* **361**, 677 (2006).
- [28] G. F. Gu and W. X. Zhou, *Phys. Rev. E* **74**, 061104 (2006).
- [29] P. Kestener and A. Arneodo, *Phys. Rev. Lett.* **91**, 194501 (2003).
- [30] E. Alessio, A. Carbone, G. Castelli, and V. Frappietro, *Eur. Phys. Jour. B* **27**, 197 (2002).
- [31] A. Carbone, G. Castelli, and H. E. Stanley, *Phys. Rev. E* **69**, 026105 (2004); A. Carbone and H. E. Stanley, *Physica A* **340**, 544 (2004)
- [32] S. Arianos and A. Carbone, *Physica A* **382**, 9 (2007).
- [33] R. H. Voss, "Random Fractal Forgeries" in NATO ASI series, Vol. F17 *Fundamental Algorithms for Computer Graphics*, edited by R. A. Earnshaw (Springer-Verlag, Berlin/Heidelberg, 1985).
- [34] W.-X. Zhou and D. Sornette, *Int. J. Mod. Phys. C* **13**, 137 (2002).
- [35] D. C. Caccia, D. Percival, M. J. Cannon, G. Raymond, J. B. Bassingthwaighte, *Physica A* **246**, 609 (1997).
- [36] K. Hu, P. Ch. Ivanov, Z. Chen, P. Carpena and H.E. Stanley, *Phys. Rev. E* **64**, 011114 (2001).
- [37] Z. Chen, P. Ch. Ivanov, K. Hu, and H.E. Stanley, *Phys. Rev. E* **65**, 041107 (2002).
- [38] L. M. Xu, P. Ch. Ivanov, K. Hu, Z. Chen, A. Carbone and H. E. Stanley, *Phys. Rev. E* **71**, 051101 (2005).
- [39] S. Stoev, M. S. Taqqu, C. Park, G. Michailidis, J. S. Marron, *Comp. Stat. and Data Analysis* **50**, 2447 (2006).
- [40] R. W. Hamming "Digital Filters", (Prentice-Hall 1998).
- [41] The source and executable files of the proposed algorithm can be downloaded at www.polito.it/noiselab/utilities .
- [42] We use the CLF algorithm included in the package FRACLAB that can be downloaded at <http://www.irccyn.ec-nantes.fr/hebergement/FracLab/>.